Monthly Notices of the ROYAL ASTRONOMICAL SOCIETY

MNRAS **540,** 2965–2974 (2025) https://doi.org/10.1093/mnras/staf926
Advance Access publication 2025 June 6

Evidence of oscillating 'compact' Comptonized corona in GRS 1915+105: insights into HFQPOs with *AstroSat*

Sreehari Harikesh [1]★ Seshadri Majumder [2] Santabrata Das [2]★ and Anuj Nandi [3]★

[1] *Department of Physics, University of Haifa, Haifa 3498838, Israel*
[2] *Indian Institute of Technology Guwahati, Guwahati 781039, India*
[3] *Space Astronomy Group, ISITE Campus, U. R. Rao Satellite Centre, Outer Ring Road, Marathahalli, Bangalore 560037, India*

Accepted 2025 May 21. Received 2025 May 21; in original form 2024 December 19

ABSTRACT

We present, for the first time, an in-depth dynamical analysis of the spectrotemporal properties of the soft variability classes (δ, κ, ω, and γ) of GRS 1915+105 during the detection of ∼70 Hz High-Frequency Quasi-periodic Oscillations (HFQPOs) using *AstroSat* data. The wide-band spectra ($0.7 - 50$ keV) are well described by thermal Comptonization along with an extended power-law component. Additionally, power spectra ($0.01 - 500$ Hz) indicate that Comptonized photons ($6 - 25$ keV) primarily contribute to the HFQPOs. Our findings reveal that high (low) count rates referred to as 'non-dips' ('dips') in the light curves of the variability classes correspond to the detection (non-detection) of HFQPOs. Accumulated 'non-dips' ('dips') spectra are modelled separately using thermal Comptonization (`nthComp`) as well as `kerrd` which indicates harder spectra and smaller inner disc radius during the detection of HFQPOs. We conduct dynamical analyses (every 32 s) to trace the presence of HFQPOs, and variations in thermal Comptonization parameters ($\Gamma_{\rm nth}$ and $\rm N_{nth}$). Moreover, we observe a positive correlation of 'non-dips' with QPO strength, HR1, and $\rm N_{nth}$, while $\Gamma_{\rm nth}$ shows an anticorrelation, suggesting that high-energy photons from the Comptonized corona are responsible for the HFQPOs. Furthermore, we estimate the size of the Comptonized corona using `kerrd` and `diskpn` to be $\sim 2.8 - 16\ r_{\rm g}$. Thus, we infer that a 'compact' oscillating corona likely modulates the high-energy radiation, exhibiting the 70 Hz HFQPOs in GRS 1915+105.

Key words: accretion, accretion discs – black hole physics – radiation mechanisms: general – X-rays: binaries – X-rays: individual: GRS 1915+105.

1 INTRODUCTION

High-frequency Quasi-periodic Oscillation (HFQPO) feature is regarded as a useful tool for understanding the accretion dynamics around black hole X-ray binaries (BH-XRBs), as they carry the imprint of strong gravity from the central source. Several BH-XRBs, such as GRS 1915+105 (Morgan, Remillard & Greiner 1997; Strohmayer 2001), GRO J1655-40 (Remillard et al. 1999), XTE J1550-564 (Homan et al. 2001), H1743-322 (Homan et al. 2005), and IGR J17091-3624 (Altamirano & Belloni 2012) were often seen to exhibit HFQPOs in the *Rossi X-ray Timing Explorer* (*RXTE*) era. Among them, GRS 1915+105 generally exhibits various structured variability classes (Belloni et al. 2000; Klein-Wolt et al. 2002; Naik, Rao & Chakrabarti 2002; Hannikainen et al. 2005, and references therein), and also demonstrates ultrafast modulations in some of these classes (Belloni et al. 2006; Belloni & Altamirano 2013). Additionally, temporal analyses of these structured variabilities often reveal HFQPOs at ∼ 70 Hz, particularly in the softer variability classes (*e.g.*, δ, γ, κ, μ, and ω), which is also confirmed by *AstroSat* (Belloni et al. 2019; Sreehari et al. 2020; Majumder et al. 2022; Majumder, Dutta & Nandi 2024).

The wide-band energy spectra of GRS 1915+105 were satisfactorily described by the thermal disc photons and non-thermal Comptonized emissions (Zdziarski et al. 2005). In fact, a disc–corona configuration was also suggested by Taam, Chen & Swank (1997); Vilhu et al. (2001), where they modelled the *RXTE* energy spectra using the multitemperature blackbody and a `powerlaw`. Vilhu & Nevalainen (1998) studied the changes of the disc temperature, optical depth, and inner disc radius of GRS 1915+105 during the rapid variations in photon count rates. Subsequently, Titarchuk & Seifina (2009) attempted to explain the energy spectra using the bulk motion Comptonization model that comprises both hard and soft thermal components. Meanwhile, the time-resolved evolution of the energy spectral parameters of this source was reported by Migliari & Belloni (2003) during its β class variability.

Indeed, the origin of HFQPOs remains of great interest as these oscillations are transient as well as subtle. However, the conclusive consensus on the origin of HFQPOs is not settled yet. In the recent past, Sreehari et al. (2020) speculated that the HFQPOs are manifested possibly due to the coherent modulation of the 'compact' Comptonized corona at the inner part of the disc. Similar findings are corroborated in some of the variability classes observed with *AstroSat* (Majumder et al. 2022, and references therein). Earlier, while studying γ class of GRS 1915+105, Belloni, Méndez & Sánchez-Fernández (2001) found HFQPOs during the low count rate ('dips') in $13 - 30$ keV energy band, although such signature disappears

★ E-mail: hjsreehari@gmail.com (SH); sbdas@iitg.ac.in (SD); anuj@ursc.gov.in (AN)

at low energies (2 − 13 keV). Meanwhile, Majumder et al. (2022) showed that when the thermal Comptonized component is dominant, HFQPOs are seen in the 'softer' variability classes ($\delta, \kappa, \omega, \gamma$) of GRS 1915+105. Following this, Majumder et al. (2024) observed that the soft photons lag behind the hard photons during detection of these HFQPOs. Majumder et al. (2025) associated HFQPOs with a larger covering fraction and increased Comptonization flux along with lower optical depth. However, there are lack of attempts to investigate the correlation between HFQPOs and the energy spectral parameters of GRS 1915+105 within structured variability classes such as κ and ω, which exhibit variations on shorter time-scales of a few tens of seconds.

Being motivated with this, in this paper, we aim to investigate the dynamical variation of the HFQPOs in different structured variability classes. To achieve our goal, we carry out a comprehensive analysis to examine the appearance and disappearance of HFQPOs within each variability class. While doing so, we consider *AstroSat* observations and make use of the short duration (32 s) data with reasonable photon statistics. With *AstroSat* data, we examine the possible correlations between the structured variabilities of the light curves and the variation of the spectral parameters to infer the origin of HFQPOs in GRS 1915+105.

The paper is organized as follows. In Section 2, we describe the selection of observations. The modelling and results are presented in Section 3. Finally, we discuss our findings and present conclusion in Section 4.

2 OBSERVATIONS

The extensive *RXTE* observations facilitated the insightful findings related to the HFQPOs of GRS 1915+105 (Morgan et al. 1997; Cui 1999; Belloni et al. 2001; Belloni & Altamirano 2013). Due to the larger collecting area, *AstroSat/LAXPC* (Antia et al. 2017) provides high quality data that allows one to carry out in-depth analyses as well as understanding of the HFQPO features. Recently, using *AstroSat/LAXPC* observations, HFQPOs are reported in several variability classes (δ, κ, γ, and ω) of GRS 1915+105 (Belloni et al. 2019; Sreehari et al. 2020; Majumder et al. 2022). In this work, we re-analyse these 'softer' variability classes between MJD 57 500 and MJD 58 050 (see Fig. 1), during which HFQPOs of $\sim$ 70 Hz frequency are observed. In particular, we choose four *AstroSat* observations corresponding to orbit numbers 3819 (δ class), 9670 (κ class), 10 394 (ω class), and 10 583 (γ class), respectively. Among these observations, κ and ω classes show structured variabilities with clear presence of high count rate ('non-dips') and low count rate ('dips') regions. Indeed, the light curves of this kind are ideally suited for studying the spectrotemporal properties of HFQPOs.

In order to examine light curves, power density spectra and energy spectra, we reduce *AstroSat* data following Agrawal et al. (2018), Sreehari et al. (2019, 2020), and Majumder et al. (2022). For timing analysis, we combine *LAXPC10* and *LAXPC20* data, whereas only *LAXPC20* data are used for spectral analysis. *AstroSat/LAXPC* light curves are generated with 1 s resolution for calculating hardness ratios using `LaxpcSoft`.[1] While generating the power density spectrum, we use *LAXPC* light curves of resolution 0.001 s. The broad-band energy spectra are generated by combining *SXT* (0.7 − 7 keV) and *LAXPC20* (3 − 50 keV) data. We also use MAXI data to study the long-term variability of the source over the duration of our interest (MJD 57 500 to MJD 58100).[2]

3 MODELLING AND RESULTS

3.1 Static imprint of variability classes

In this work, we use *AstroSat/LAXPC* observations to investigate the origin and characteristics of $\sim$ 70 Hz HFQPOs detected in GRS 1915+105. We identify four variability classes (*i.e.*, δ, κ, ω, and γ classes), where HFQPOs are observed (Sreehari et al. 2020; Majumder et al. 2022). In Figs 1(a) and (b), we present the MAXI light curve (2 − 20 keV) and the hardness ratio (HR: 6 − 20 keV/2 − 6 keV) of GRS 1915+105 during *AstroSat* observations. The HR variation evidently indicates that the source remains in the 'softer' spectral states. The vertical dashed lines denote different variability classes, and the corresponding light curves are presented at the inset of Fig. 1(a).

We generate deadtime corrected and Poisson noise subtracted PDS (see Agrawal et al. 2018; Sreehari et al. 2020, for details) of GRS 1915+105. In Fig. 1(c), we depict PDS of the source for ω class (see Table 1) in wide frequency band (0.01 − 500 Hz). The HFQPO feature is modelled using a `Lorentzian` with a centroid frequency of 68.09 Hz, a Q factor ($\nu/\Delta\nu$) of 12.26 and a significance ($\sigma = \mathrm{norm}/\mathrm{err_{neg}}$) of 5.62. The insets show the PDS across different energy ranges, revealing that HFQPO is detected only in the 6 − 25 keV range, without detection of HFQPO in the 3 − 6 keV and 25 − 60 keV bands (see also Sreehari et al. 2020; Majumder et al. 2022).

Subsequently, we perform broad-band spectral modelling combining both *SXT* (Singh et al. 2017) data (0.7 − 7 keV) and *LAXPC20* (3 − 50 keV) data for all variability classes under consideration. Initially, the broad-band spectra are modelled using phenomenological model combination of `constant*Tbabs*edge*smedge*(diskbb+powerlaw)`. The `edge` component corresponds to Xenon absorption around 29 − 32 keV (Sreehari et al. 2020; Majumder et al. 2022), whereas the `smedge` component accounts for an absorption feature around 8 keV which primarily depends on the disc inclination and ionization parameters (Ross, Fabian & Brandt 1996). We use `gain fit` command to take care of residuals due to instrumental features at 1.8 and 2.2 keV of *SXT*. The best-fitting modelling yields the `diskbb` inner disc temperature $kT_{\rm in} \sim 2.72$ keV and `powerlaw` photon index $\Gamma \sim 2.73$.

Further, we model the broad-band energy spectra using physical model components to examine the characteristics of the thermally Comptonized emissions. Accordingly, we adopt a model combination `Tbabs*edge*smedge(nthComp+powerlaw)` (hereafter Model-1), where we fix the disc blackbody temperature as 0.1 keV for seed photons. The unfolded energy spectrum along with residuals of ω class is shown in Fig. 1(d), where the energy range of dominant Comptonization is highlighted using grey shade. We find that the photon index of the thermal Comptonization component ranges as $\Gamma_{\rm nth} \sim 1.68 - 1.92$, electron temperature $kT_{\rm e} \sim 2.41 - 2.62$ keV and `powerlaw` photon index $\Gamma_{\rm PL} \sim 2.14 - 3.15$. The model fitted parameters are tabulated in Table 1. In case of ω class (Orbit 10394), the broad-band fit of `nthComp` model without the additional `powerlaw` resulted in a reduced chi-squared of $1328/627 = 2.11$. After adding the `powerlaw`, the reduced chi-squared improved to $724/625 = 1.15$ justifying the need for the `powerlaw` component.

[1] https://www.tifr.res.in/~astrosat_laxpc/LaxpcSoft.html

[2] http://maxi.riken.jp/top/index.html

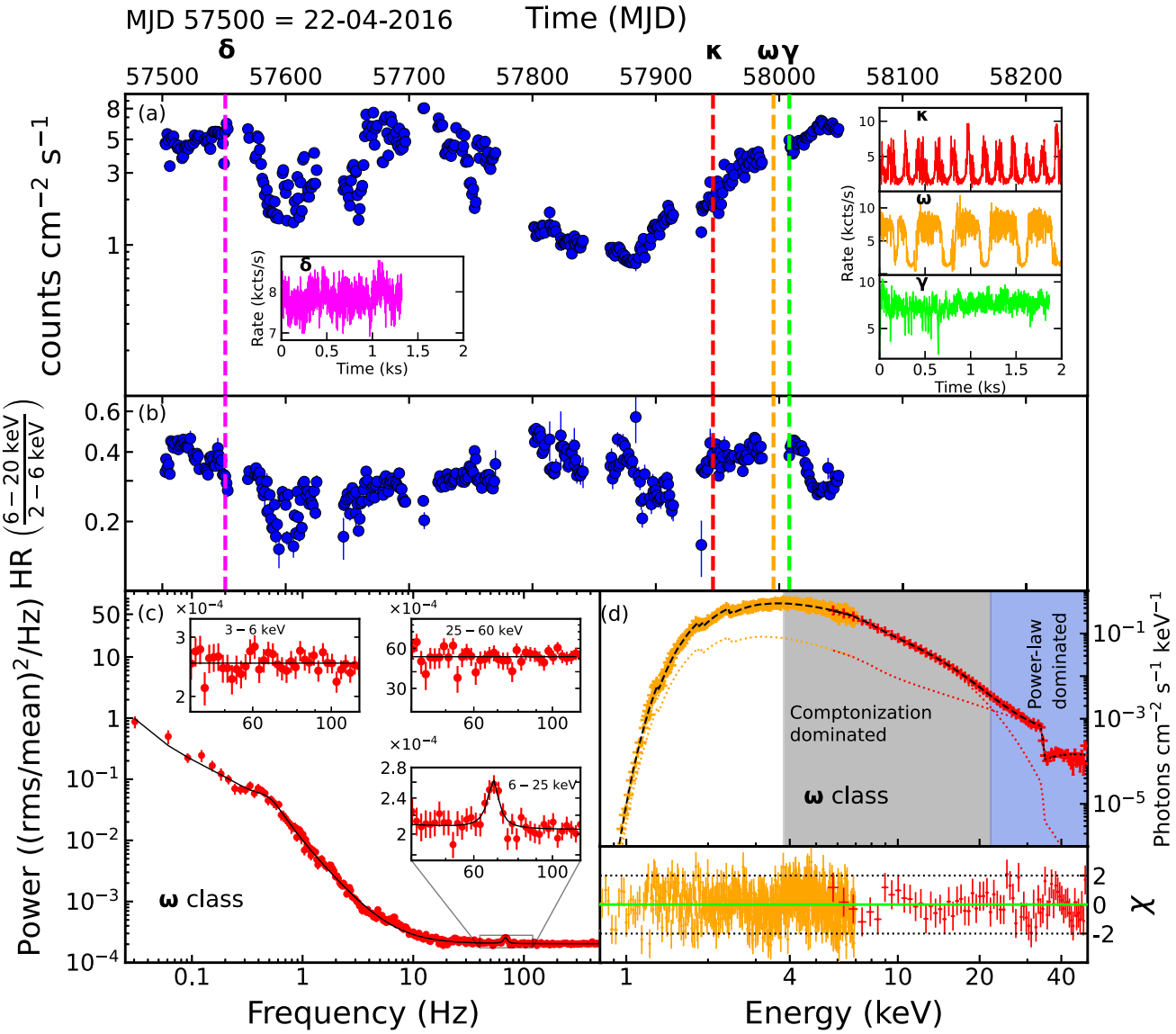

Figure 1. Variation of (a) photon count rate as observed with *MAXI* and (b) the hardness ratio (HR) with time. Dashed vertical lines denote different variability classes as observed by *AstroSat* and the corresponding light curves are shown at the inset of panel (a). (c) Power spectral distribution in rms-frequency space is plotted for ω class observation (Orbit 10394, MJD 57995.40). At the insets, PDS in different energy band are shown. The broad-band spectrum of ω class modelled using `constant*Tbabs*edge*smedge(nthComp+powerlaw)` is presented in panel (d). The y-axis of all the four main panels are in logarithmic scale. See the text for details.

This additional `powerlaw` indicates the presence of an extended corona besides the thermally Comptonized cloud represented by `nthComp`. The relatively higher values of photon-index ($\sim 2.14 - 3.15$) of this `powerlaw` component can be attributed to non-thermal processes such as bulk motion Comptonization (Niedźwiecki & Zdziarski 2006; Titarchuk & Seifina 2009). It may be noted that without the `smedge` (`edge`) component, Model-1 resulted in a fit with a $\chi^2_{\rm red}$ of 1.46(1.44), justifying the inclusion of these absorption model components.

We continue modelling the source spectra replacing `diskbb` by `diskpn` (Gierliński et al. 1999) using model combination `Tbabs*edge*smedge(diskpn+powerlaw)` (hereafter Model-2) to estimate the size of the corona. Considering distance, mass, and inclination of the source as 8.6 kpc, 12.4 $M_\odot$ (Reid et al. 2014; Sreehari et al. 2020), and 65° (Zdziarski 2014), the inner disc radius is computed as $R_{\rm in} \sim 14.62 - 16.56\ r_{\rm g}$, where $r_{\rm g}$ is the gravitational radius. To examine the relativistic effects, we use `kerrd` (Ebisawa et al. 2003) model instead of `diskbb` as `constant*Tbabs*edge*smedge(kerrd+powerlaw)` (hereafter Model-3) while computing $R_{\rm in}$. The source parameters such as distance, mass, and inclination are fixed in Model-3 to the above mentioned values. Since `kerrd` model is developed considering black hole of spin $a_{\rm k} = 0.998$, we obtain the inner disc radius very close to the horizon as $R_{\rm in} \sim 3.27 - 3.72\ r_{\rm g}$. Based on the findings from Model-2 and Model-3, we infer that the inner disc radius (equivalently size of the corona) seems to be localized in the range $3\ r_{\rm g} \lesssim R_{\rm in} \lesssim 16\ r_{\rm g}$. The best-fitting parameters for both models are presented in Table 1. In this study, we exclude Model-2 from further analysis as it uses the pseudo-Newtonian approach to approximate gravitational effects, rather than using the general

Table 1. The parameters obtained from broad-band (0.7 − 50 keV) spectral modelling (average) of the *AstroSat* observations of δ, κ, ω, and γ classes of GRS 1915+105 are tabulated. Three different model combinations are used as Model-1: `constant*Tbabs*edge*smedge(nthComp+powerlaw)`, Model-2: `Tbabs*edge*smedge(diskpn+powerlaw)`, and Model-3: `Tbabs*edge*smedge(kerrd+powerlaw)`. The bolometric X-ray luminosities are computed in 1 − 100 keV energy band. See the text for details.

MJD (Orbit)	Class (ν_{QPO} Hz)	Model-1				Model-2			Model-3				
		Γ_{nth}	Γ_{PL}	χ^2_{red} (χ^2/dof)	R_{in} (r_g)	T_{max} (keV)	Γ	χ^2_{red} (χ^2/dof)	R_{in} (r_g)	Γ	χ^2_{red} (χ^2/dof)	L_{bol} (L_{Edd})	L^D_{bol} (L_{Edd})	L^N_{bol} (L_{Edd})
57551.04 (3819)	δ (69.18)	1.82 ± 0.21	3.15 ± 0.23	56/61	14.9 ± 2	2.77 ± 0.01	3.23 ± 0.01	54/62	$3.72^{+0.18}_{-0.18}$	$2.82^{+0.09}_{-0.04}$	0.90 (50/55)	0.18	–	–
57946.34 (9670)	κ (70.45)	1.87 ± 0.05	2.14 ± 0.55	733/601	14.62 ± 0.29	2.59 ± 0.01	2.91 ± 0.01	716/598	$3.56^{+0.12}_{-0.22}$	3.02 ± 0.01	1.22 (738/601)	0.10	0.07	0.15
57995.40 (10394)	ω (68.09)	1.68 ± 0.08	2.41 ± 0.38	724/625	16.56 ± 0.23	2.75 ± 0.01	2.77 ± 0.01	712/628	$3.27^{+0.09}_{-0.09}$	2.76 ± 0.01	1.08 (682/630)	0.19	0.09	0.26
58008.18 (10583)	γ (72.32)	1.92 ± 0.11	2.61 ± 0.58	604/534	15.49 ± 0.35	2.84 ± 0.01	2.93 ± 0.01	556/533	$3.58^{+0.08}_{-0.05}$	$2.92^{+0.02}_{-0.01}$	1.02 (546/535)	0.25	–	–

relativistic prescription. However, we utilize Model-2 solely to estimate the maximum inner disc radius that suggests the largest plausible corona geometry.

Further, to examine the variations in spectral parameters during 'dips' and 'non-dips' independently, we generate separate broad-band spectra combining good time intervals (gti) of only the 'dips' ('non-dips') for simultaneous *LAXPC* and *SXT* observations. This analysis is carried out independently for ω and κ class observations only as they exhibit distinct 'dips' and 'non-dips' in the light curve unlike other classes. The resulting broad-band spectra are shown in Fig. 2 and the best-fitted spectral parameters with Model-1 are tabulated in Table 2. N_{nth} and N_{PL} denote the normalization of the `nthComp` and `powerlaw` components, respectively. We observe distinct variations in spectral parameters during 'dips' and 'non-dips'. For instance, the photon index of thermal Comptonization remains harder ($\Gamma_{nth} \sim 1.78$) during 'non-dips' and it steepens ($\Gamma_{nth} \sim 2.06$) during 'dips' indicating softening of spectra. We present the results of Model-3 in Table 2. While Γ is in the range $2.14 - 2.54$, the inner disc radius R_{in} is low ($2.87 - 2.93 r_g$) for 'non-dips' compared to 'dips' ($5.35 - 6.69 r_g$). We explore these effects further with our dynamic spectral analysis using *LAXPC* data in Section 3.2.

In addition, we generate the MCMC (Markov Chain Monte Carlo) chains associated with the best-fitted spectral parameters of 'dips' and 'non-dips' spectra in XSPEC. Contour plots were produced from these chains to check the correlations between spectral parameters, which are presented in Figs 3 and 4 for ω class (Orbit 10394) observations for 'dips' and 'non-dips' segments. In Model-1, the spectrum consists of two additive components, namely `powerlaw` and `nthComp`. During the 'dips' (see Fig. 3), the `powerlaw` parameters (Γ_{PL} and N_{PL}) exhibit a positive correlation with each other, while both show an anticorrelation with the `nthComp` parameters (Γ_{nth}, kT_e, and N_{nth}). Furthermore, the `nthComp` parameters are themselves mutually correlated. A similar pattern of correlations among these parameters is observed during the 'non-dips' segments as well (see Fig. 4). However, notable difference between the spectra are observed with 'non-dips' exhibiting harder spectral distribution (lower Γ_{nth}) and higher normalizations for both `nthComp` and `powerlaw` components (N_{nth} and N_{PL}), respectively.

3.2 Dynamical spectrotemporal properties

Exploring the dynamic nature of structured variability classes enhances our understanding of the origins of HFQPOs. Following Majumder et al. (2022), we generate dynamic power spectra using STINGRAY[3] package (Huppenkothen et al. 2019), where the span of time segments is considered as 32 s and the frequency bin size is chosen as 1 Hz. We apply 'bicubic' interpolation method to smoothen out the PDS for plotting, as it is less noisy compared to other options such as 'sinc', and 'spline'. 'Bicubic' interpolation uses a weighted average approach by fitting cubic polynomials to 16 neighbouring pixels that form a 4×4 square around the pixel under consideration to compute its value, thus reducing artefacts such as pixelation or jagged edges. The obtained results are presented in the second panels of Fig. 5 for ω class (left side) and κ class (right side). The colour-coded dynamic PDS indicates that dark red represents a strong signal, gradually fading to yellow as the signal strength decreases. The corresponding light curves from ω and κ classes are shown in the top panels of Fig. 5. It is evident from these light curves that there

[3] https://pypi.org/project/stingray/

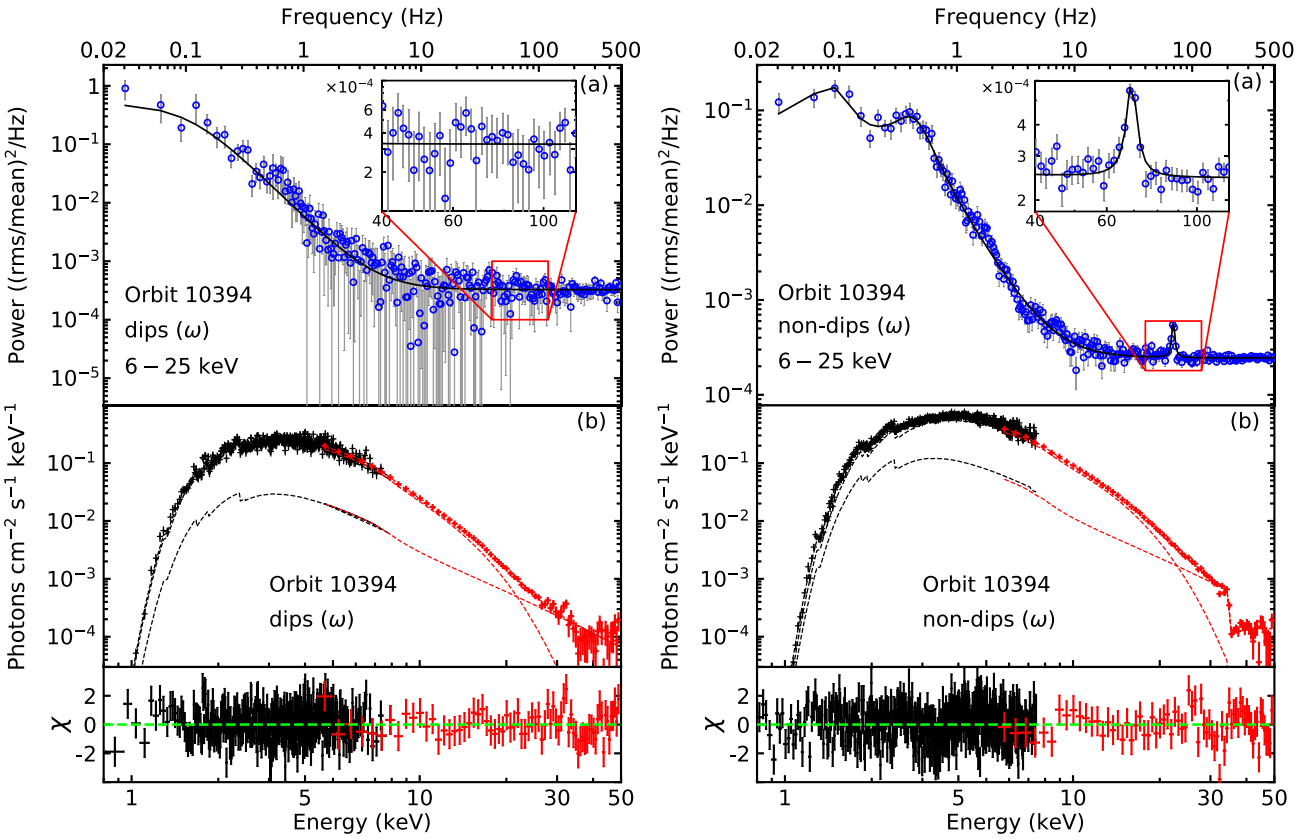

Figure 2. Left: Power density spectrum (PDS) and energy spectral distribution obtained by co-adding data from the 'dips' segments of the light curve in the ω class (orbit 10394) of GRS 1915 + 105 are shown in the top and bottom panels, respectively. Right: Corresponding results obtained from the 'non-dips' segments of the light curve. See the text for details.

is significant oscillation in the high count-rate regions as opposed to the low count-rate regions. In the third and fourth panels of Fig. 5, we present the hardness ratios HR1 and HR2, where HR1 is defined as the ratio of flux in $6-15$ to $3-6$ keV, whereas HR2 is the ratio of flux in $15-60$ to $3-6$ keV. It is evident from the figure that HFQPOs are generally detected when the photon count rates are higher ('non-dips') in both ω and κ variability classes. Further, HR1 is also seen to correlate with the photon count rates, however no such correlation is observed for HR2.

We further examine the time-dependent behaviour of the energy spectrum. In doing so, we model the energy spectrum in $3-25$ keV energy range using Model-1 for each successive 32 s time segment within the *AstroSat* observations. Here, we restrict the energy range upto 25 keV in order to avoid poor photon statistics at higher energies and hence `powerlaw` component is excluded while model fitting. The results are illustrated in 5^{th} and 6^{th} panels of Fig. 5, depicting the time evolution of photon index (Γ_{nth}) and normalization (N_{nth}) from the `nthComp` component of Model-1. We observe that Γ_{nth} generally exhibits an anticorrelation with the photon count rate, while N_{nth} aligns with the variations in the count rate. We also note that HFQPOs disappear when Γ_{nth} is higher. Notably, when HFQPOs are detected, R_{in} estimated from the `kerrd` component of Model-3 is found to extend at relatively smaller radii (see 7^{th} panel of Fig. 5) compared to the scenario when HFQPOs are absent. Similar variation of R_{in} w.r.t. count rate variations were reported by Migliari & Belloni (2003) though it was not in the context of HFQPOs. The comparatively larger uncertainty in radius estimates during dips has to do with low photon statistics in the spectrum corresponding to that 32 s interval. This observation highlights that HFQPO features are directly associated with higher HR1 values and lower Γ_{nth}, indicating relatively harder spectral states. It is worth noting that the count rates for the δ and γ classes remain consistently high, resulting in stable spectral parameters (see Sreehari et al. 2020; Majumder et al. 2022).

Next, we estimate the source bolometric luminosity (L_{bol}) in $1-100$ keV energy range as $L_{bol} = 4\pi d^2 F$, where d (= 8.6 kpc) refers to the source distance and F denotes the X-ray flux. For ω class observation (Orbit 10394), we obtain $L_{bol} = 0.19\ L_{Edd}$, where L_{Edd} ($= 1.26 \times 10^{38} (M_{BH}/M_\odot)$ ergs s^{-1}) is the Eddington Luminosity and M_{BH} ($= 12.4\ M_\odot$) is the black hole mass. Further, we independently calculate the bolometric luminosity by adding (a) all the dip segments (low count; L^D_{bol}) and (b) all the non-dip segments (high count; L^N_{bol}) of the structured variability classes (ω and κ). For ω class, we obtain $L^D_{bol} = 0.09\ L_{Edd}$ and $L^N_{bol} = 0.26\ L_{Edd}$, whereas for κ class, $L^D_{bol} = 0.07\ L_{Edd}$ and $L^N_{bol} = 0.15\ L_{Edd}$. With this, we infer that HFQPOs seem to be associated with the relatively high source luminosity (see bottom panels of Fig. 5). We also calculate L_{bol} for δ class (Orbit 3819) and γ class (Orbit 10583) observation. All the obtained results are presented in Table 1.

4 DISCUSSION AND CONCLUSION

In this paper, for the first time, we trace the dynamical evolution of timing and spectral properties of GRS 1915+105 in small time segments (32 s) of the structured variability classes exhibiting $\sim$ 70 Hz HFQPO feature. We use *AstroSat* observations in the softer variability classes, namely δ, κ, ω, and γ classes. We find that for

Table 2. Broad-band (0.7 − 50 keV) spectral parameters for accumulated 'dips' and 'non-dips' segments. Here, adopted models are as Model-1: `Tbabs*edge*smedge (nthComp+powerlaw)` and Model-3: `Tbabs*edge*smedge (kerrd+powerlaw)`. See the text for details.

Orbit	Class	Γ_{nth}	N_{nth}	Γ_{PL}	Model-1 N_{PL}	smedge (keV)	kT_e (keV)	(χ^2/dof)	$R_{in}(r_g)$	N_{kerr}	Model-3 Γ	N_{PL}	(χ^2/dof)
9670	κ (non-dips)	1.77 ± 0.10	6±2	2.34 ± 0.18	1.49±1.1	7.7 ± 0.2	2.89 ± 0.18	583/550	2.87±0.64	0.35±0.07	$2.54^{+0.22}_{-0.23}$	4.1±0.1	576/544
9670	κ (dips)	1.99 ± 0.06	5.6±0.9	2.14 ± 0.47	$0.17^{+0.39}_{-0.14}$	7.5 ± 0.2	2.13 ± 0.11	557/528	$6.69^{+0.15}_{-1.66}$	0.10±0.01	$3.40^{+0.16}_{-0.25}$	18.9±0.4	586/529
10394	ω (non-dips)	1.78 ± 0.09	10±1	2.53 ±0.22	6±3	7.7 ± 0.2	2.5 ± 0.1	723/627	$2.93^{+0.59}_{-0.59}$	0.59±0.12	$2.27^{+0.16}_{-0.47}$	3.4±0.1	657/610
10394	ω (dips)	2.06 ± 0.17	6±2	2.54 ± 0.25	1.3±0.1	7.5 ± 0.3	2.5 ± 0.1	436/443	5.35±0.69	0.06±0.01	$3.50^{+0.08}_{-0.24}$	42±17	429/442

ω and κ classes, power of ν_{QPO}, HR1 and L_{bol} correlate with the high count rates ('non-dips'), while Γ_{nth} and R_{in} generally show anticorrelation.

Wide band (0.7 − 50 keV) spectral modelling of the 'softer' variability classes of GRS 1915+105 indicates the presence of both thermal Comptonization component ($\Gamma_{nth} \sim 1.68 - 1.92$) and `powerlaw` component ($\Gamma_{PL} \sim 2.14 - 3.15$) (see Sreehari et al. 2020; Majumder et al. 2022, for more details). These findings seem to mimic the existence of two Comptonized components as reported by Titarchuk & Seifina (2009). To explore the variations further, we considered ω and κ classes where the flux alters between intervals of 'dips' and 'non-dips'. All the 'dips' segments were combined, resulting in a broad-band spectrum with a photon index of $\Gamma_{nth} \sim 2.06$. In comparison, the accumulated 'non-dips' segments yield a comparatively harder spectrum with $\Gamma_{nth} \sim 1.78$ for the ω class. The `powerlaw` index remains same ~ 2.5 for both 'dips' and 'non-dips' segments. With Model-3, we obtained an inner disc radius $< 3\ r_g$ for 'non-dips' and $\sim 6r_g$ for 'dips'. We associate the inner disc radius with the size of a Compton corona that is possibly present between the black hole and the disc. Contour plots of Model-1 (see Figs 3 and 4) indicate that the `powerlaw` parameters are mutually correlated with each other, while they are anticorrelated with the `nthComp` parameters. It is worth mentioning that though 'dips' and 'non-dips' parameters show similar trends of correlation, the 'non-dips' spectra are harder (lower Γ_{nth}) and have higher normalization (N_{nth}).

Notably, from a dynamic analyses of the *LAXPC* (3−25 keV) energy spectra (divided into 32 s segments within each observation duration), we infer that the source spectral nature is softer ($\Gamma_{nth} \gtrsim 2.2$, HR1 $\lesssim 0.7$) for the 'dips' segments, whereas for 'non-dips' segments, the spectra appear to be harder ($\Gamma_{nth} \lesssim 2$, HR1 $\gtrsim 1$) (see Fig. 5). Moreover, we observe that the strength of HFQPOs are directly correlated with the photon count rates. It is important to note that the dynamic energy spectra are modelled using the `nthComp` component alone, as high-quality spectral data with sufficient photon counts in short durations are available only up to 25 keV. We binned the data at 32 s to facilitate the analysis of dynamics at shorter time-scales. This enables us to estimate the contribution from thermal Comptonization without `powerlaw` component. Evidently, the existence of HFQPOs is associated with the regions that inverse Comptonizes the soft photons to produce high energy radiations (see also Fig. 1d). Interestingly, δ and γ classes do not show any structural variability in the light curves, however, their luminosities (L_{bol}) are comparable with L^N_{bol} of ω and κ classes (see Table 1).

Meanwhile, several models were proposed to explain the HFQPOs observed from GRS 1915+105. Cui, Zhang & Chen (1998) and Merloni et al. (1999) proposed the relativistic precession model (RPM), where the orbital plane of the accreting particles do not align with the equatorial plane of the rotating black hole due to the relativistic frame-dragging effects. Nowak et al. (1997) and Morgan et al. (1997) also attempted to explain the origin of HFQPOs in GRS 1915+105 based on the 'diskoseismic' g-mode oscillation originally introduced by Kato & Fukue (1980) for Newtonian discs. Further, Kato (2004) proposed that HFQPOs in GRS 1915+105 may result from resonances between disc oscillation modes and internal disc warps. Following this, Kotrlová et al. (2020) investigated the influence of non-geodesic forces, such as magnetic fields and radiation pressure on epicyclic frequencies, concluding that several models are incompatible with rapidly spinning systems like GRO J1655-40 and GRS 1915+105. Their findings favour pressure-supported disc oscillations as a viable explanation for HFQPOs. More recently, Musoke et al. (2023) employed 3D GRMHD simulations

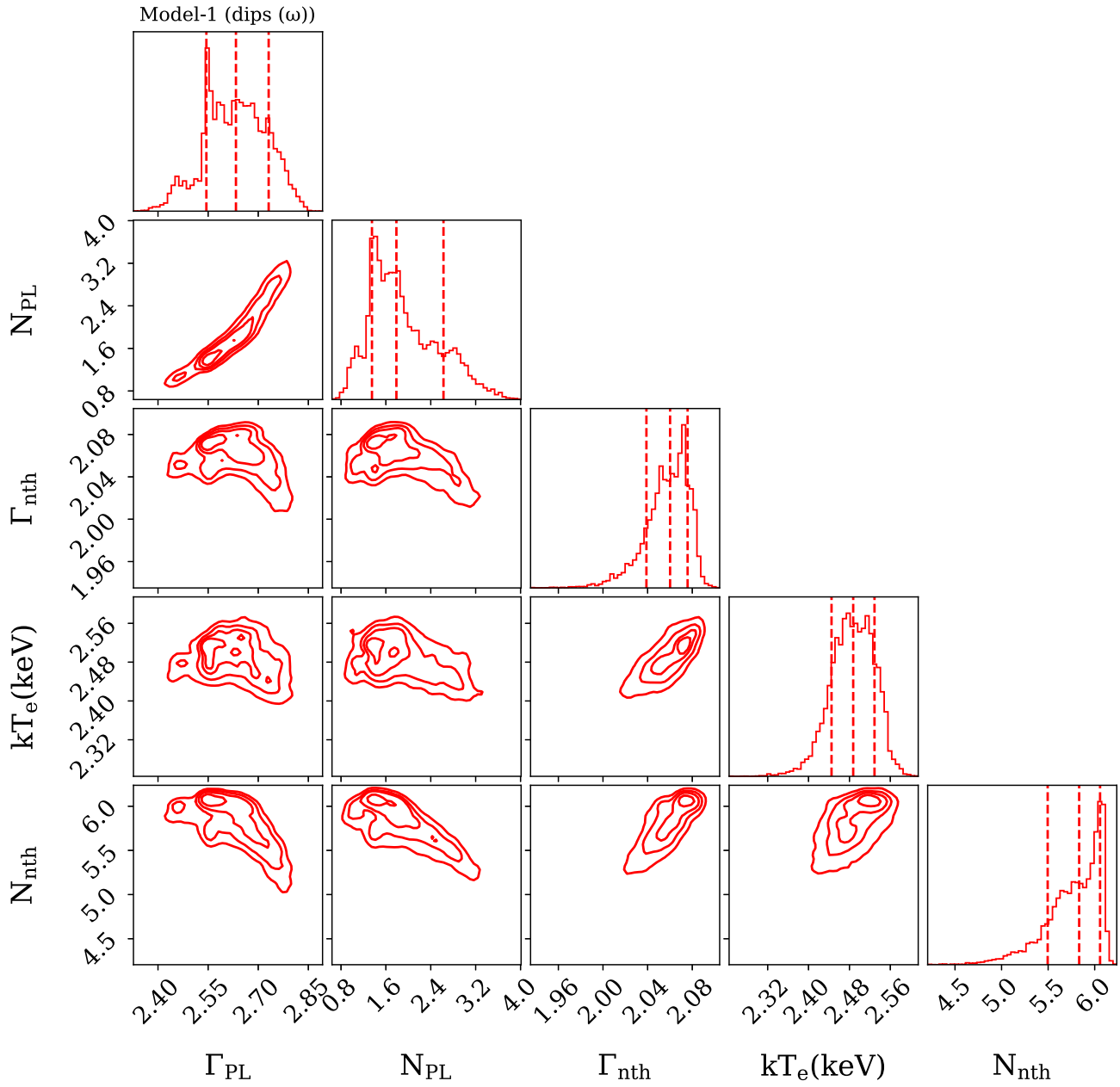

Figure 3. Correlations between parameters of `nthComp` and `powerlaw` components of Model-1 are presented for the 'dips' segment of the ω class variability. In addition to the contours, we also show the distribution of each parameter on the top. The `powerlaw` parameters, such as Γ_{PL} and N_{PL}, are positively correlated and both of them are anticorrelated with the `nthComp` parameters (Γ_{nth}, kT_e, and N_{nth}). See the text for details.

to associate HFQPOs with radial epicyclic oscillations of a dense gas ring near the tearing radius, demonstrating that disc tearing and precession can plausibly generate a higher frequency QPO feature. Moreover, Dhaka et al. (2023) reported the possible origin of QPO based on the relativistic dynamical frequency model. Meanwhile, Dihingia et al. (2019) indicates that the modulation of the compact inner disc (equivalently Comptonized corona) successfully exhibits the quasi-periodic variations of the emergent flux from a viscous accretion flow.

In addition, there were attempts to explain the structured variability classes (ω, κ, λ, and ρ), characterized by recurring 'dip' and 'non-dip' segments, in the light curves of GRS 1915+105 using accretion instability models. These models attribute the variability to rapid evacuation and subsequent gradual refilling of the inner accretion disc driven by viscous-thermal instabilities (Belloni et al. 1997; Neilsen, Remillard & Lee 2011; Vincentelli et al. 2023). Meanwhile, Janiuk, Czerny & Siemiginowska (2000) demonstrated that the radiation pressure-driven instability within a standard accretion disc model can account for the intricate temporal variability observed in GRS 1915+105. However, using a model-independent approach, Nandi et al. (2001) and Chakrabarti et al. (2005) suggested that these changes are likely to be associated with the sub-Keplerian accretion flow, as the observed transition time-scales are much shorter than the expected viscous time-scale. Furthermore, GRS 1915 + 105 has

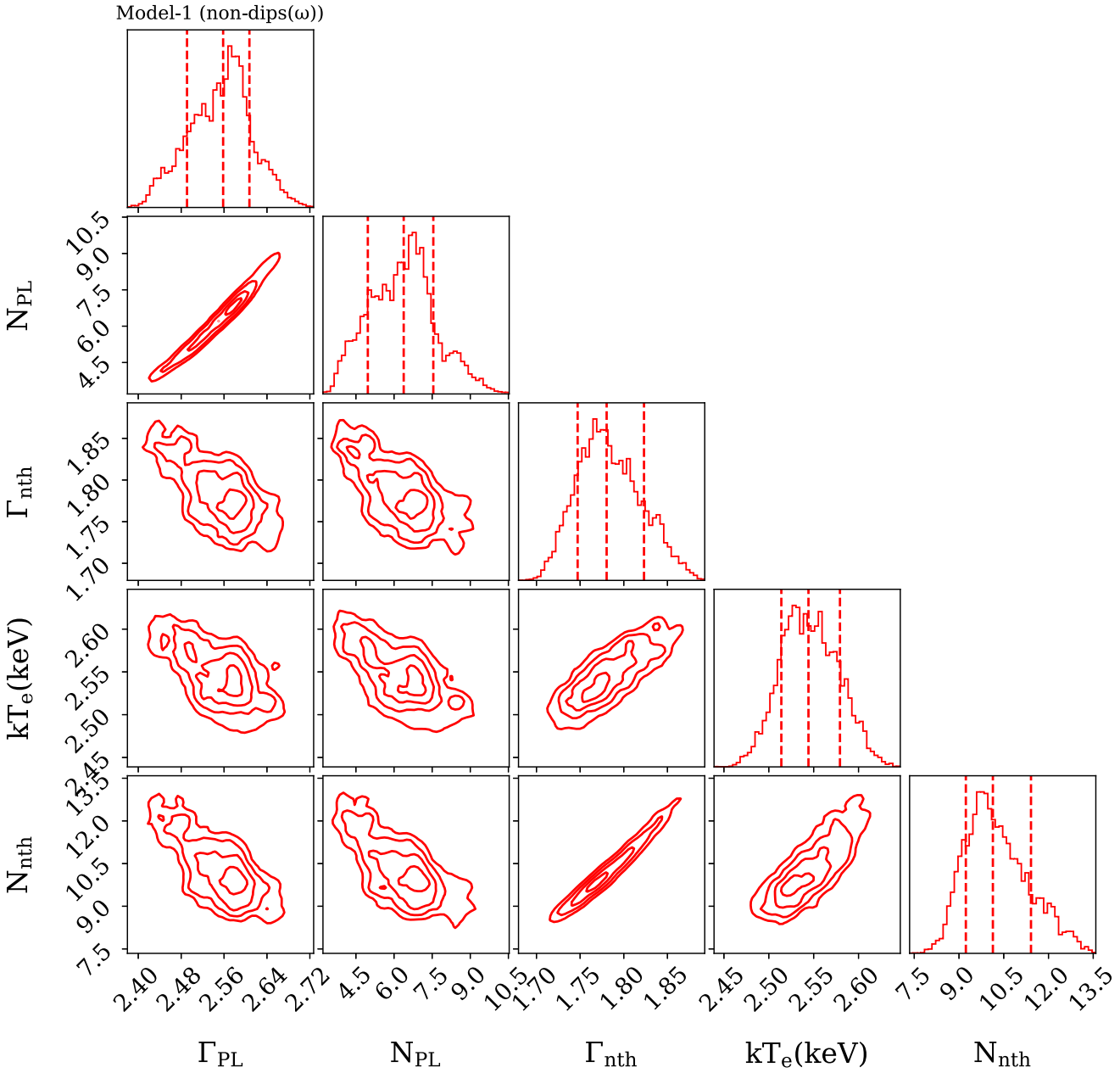

Figure 4. Same as Fig. 3, but for 'non-dips' segments. See the text for details.

been observed to display variability and class transitions over a wide luminosity range ($0.7 - 35$ per cent of $L_{\rm Edd}$) (Athulya et al. 2022; Athulya & Nandi 2023), indicating that such variability can occur without the inner disc evacuation as proposed by disc instability models, and largely independent of the accretion rate.

Overall, the present dynamic spectrotemporal analysis of ω and κ variability classes in GRS 1915 + 105 reveals a clear association between inner disc radius variations and the presence of HFQPOs. We find that HFQPOs at ~ 70 Hz occur only during relatively harder spectral states ($\Gamma_{\rm nth} \lesssim 2$), where the inner disc is close to the black hole ($R_{\rm in} \lesssim 4r_g$), suggesting a compact Comptonizing corona. Conversely, in softer states ($\Gamma_{\rm nth} \gtrsim 2.2$) with larger inner disc radii ($R_{\rm in} \gtrsim 7r_g$), the HFQPOs are absent. Spectral modelling using `kerrd` and `diskpn` components constrains the maximum inner disc radius as $\sim 16r_{\rm g}$, further supporting a link between disc truncation and corona size. Collectively, the observed dynamic variations in photon index, spectral hardness, inner disc radius, and the presence or absence of HFQPOs support the interpretation that these oscillations result from aperiodic modulations in a compact, high-energy Comptonized corona. Since the observed modulations occur on timescales shorter than the viscous time-scale, a sub-Keplerian accretion flow likely governs this behaviour. This conjecture possibly aligns with theoretical prescription where the coronal structures and their associated variabilities are the natural consequences of sub-Keplerian accretion under appropriate physical conditions (Chakrabarti & Titarchuk 1995; Das et al. 2014; Suková & Janiuk 2015; Debnath, Chattopadhyay & Joshi 2024).

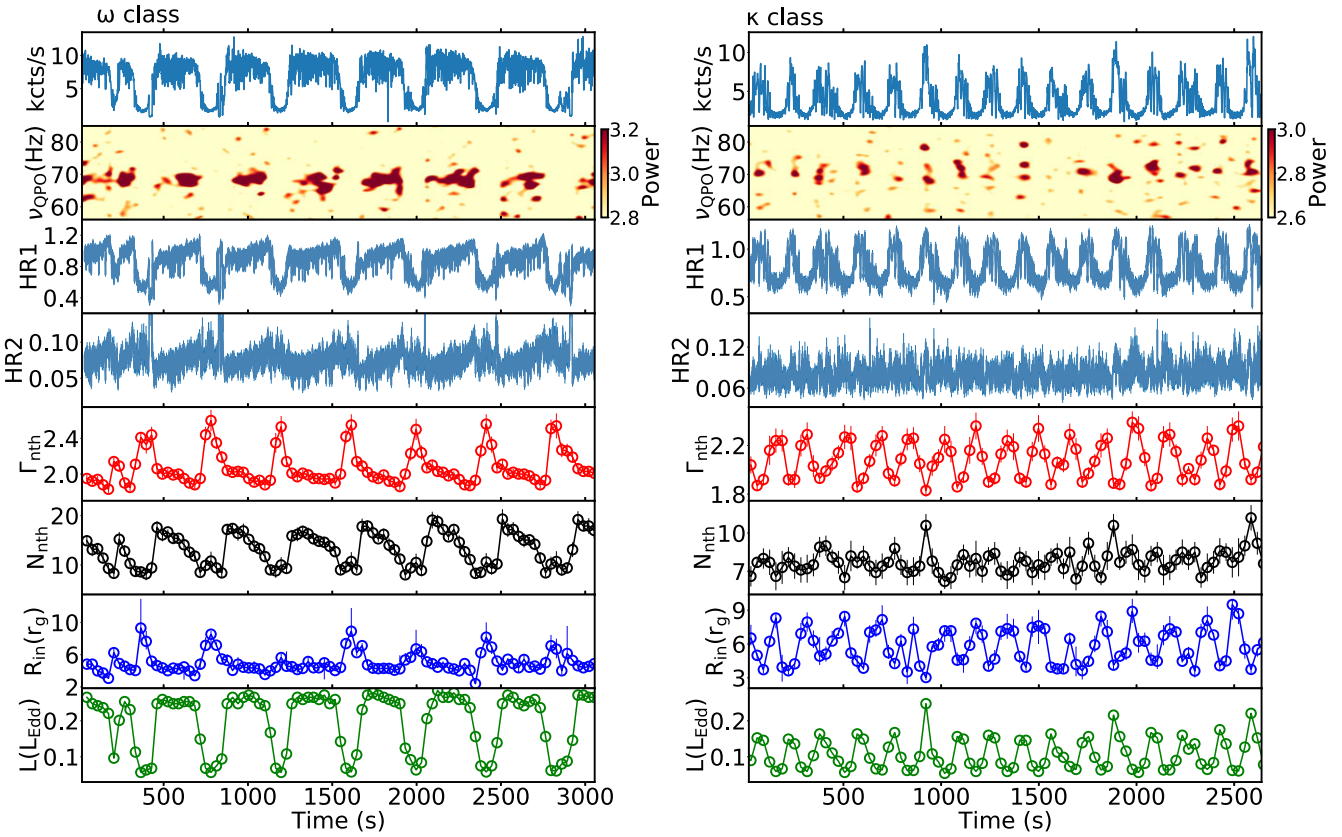

Figure 5. Dynamical variation of spectrotemporal parameters for ω class (*left*) and κ class (*right*) are shown. The count rate (kcts s^{-1}), ν_{QPO} (Hz), HR1, HR2, Γ_{nth}, N_{nth}, $R_{in}(r_g)$, and L (L$_{Edd}$) are presented successively from top to bottom panels for ω and κ classes. The spectral parameters are derived from Model-1 for Γ_{nth} and N_{nth}, and from Model-3 for R_{in}. Here, Γ_{nth} and R_{in} are anticorrelated with count rate, meanwhile all other quantities except HR2 are correlated with count rate. The dynamic PDS in the second panel has a frequency binning of 1 Hz and it uses 'bicubic' interpolation for visualization. See the text for details.

ACKNOWLEDGEMENTS

The authors are thankful to the reviewer for his/her valuable suggestions and comments that helped to improve the quality of the manuscript. SH acknowledges support from Prof. Doron Chelouche of the Department of Physics, University of Haifa through grants from the Israeli Science Foundation (ISF 2398/19, 1650/23). AN thanks GH, SAG; DD, PDMSA; and Director, URSC for encouragement and continuous support to carry out this research. This research made use of the data obtained from the *AstroSat* archive of the Indian Space Science Data Center (ISSDC). The authors thank the SXT-POC of TIFR and the *LAXPC* team of IUCAA and TIFR for providing the data extraction software for the respective instruments.

DATA AVAILABILITY

Data used for this publication are currently available at the Astrobrowse (*AstroSat* archive) website (https://astrobrowse.issdc.gov.in/astro_archive/archive) of the Indian Space Science Data Center (ISSDC).

REFERENCES

Agrawal V. K., Nandi A., Girish V., Ramadevi M. C., 2018, MNRAS, 477, 5437
Altamirano D., Belloni T., 2012, ApJ, 747, L4
Antia H. M. et al., 2017, ApJS, 231, 10
Athulya M. P., Nandi A., 2023, MNRAS, 525, 489
Athulya M. P., Radhika D., Agrawal V. K., Ravishankar B. T., Naik S., Mandal S., Nandi A., 2022, MNRAS, 510, 3019
Belloni T. M., Altamirano D., 2013, MNRAS, 432, 10
Belloni T., Méndez M., King A. R., van der Klis M., van Paradijs J., 1997, ApJ, 488, L109
Belloni T., Klein-Wolt M., Méndez M., van der Klis M., van Paradijs J., 2000, A&A, 355, 271
Belloni T., Méndez M., Sánchez-Fernández C., 2001, A&A, 372, 551
Belloni T., Soleri P., Casella P., Méndez M., Migliari S., 2006, MNRAS, 369, 305
Belloni T. M., Bhattacharya D., Caccese P., Bhalerao V., Vadawale S., Yadav J. S., 2019, MNRAS, 489, 1037
Chakrabarti S., Titarchuk L. G., 1995, ApJ, 455, 623
Chakrabarti S. K., Nandi A., Chatterjee A. K., Choudhury A. K., Chatterjee U., 2005, A&A, 431, 825
Cui W., 1999, ApJ, 524, L59
Cui W., Zhang S. N., Chen W., 1998, ApJ, 492, L53
Das S., Chattopadhyay I., Nandi A., Molteni D., 2014, MNRAS, 442, 251
Debnath S., Chattopadhyay I., Joshi R. K., 2024, MNRAS, 528, 3964
Dhaka R., Misra R., Yadav J. S., Jain P., 2023, MNRAS, 524, 2721
Dihingia I. K., Das S., Maity D., Nandi A., 2019, MNRAS, 488, 2412
Ebisawa K., Życki P., Kubota A., Mizuno T., Watarai K.-y., 2003, ApJ, 597, 780
Gierliński M., Zdziarski A. A., Poutanen J., Coppi P. S., Ebisawa K., Johnson W. N., 1999, MNRAS, 309, 496
Hannikainen D. C. et al., 2005, A&A, 435, 995
Homan J., Wijnands R., van der Klis M., Belloni T., van Paradijs J., Klein-Wolt M., Fender R., Méndez M., 2001, ApJS, 132, 377

Homan J., Miller J. M., Wijnands R., van der Klis M., Belloni T., Steeghs D., Lewin W. H. G., 2005, ApJ, 623, 383
Huppenkothen D. et al., 2019, ApJ, 881, 39
Janiuk A., Czerny B., Siemiginowska A., 2000, ApJ, 542, L33
Kato S., 2004, PASJ, 56, L25
Kato S., Fukue J., 1980, PASJ, 32, 377
Klein-Wolt M., Fender R. P., Pooley G. G., Belloni T., Migliari S., Morgan E. H., van der Klis M., 2002, MNRAS, 331, 745
Kotrlová A. et al., 2020, A&A, 643, A31
Majumder S., Sreehari H., Aftab N., Katoch T., Das S., Nandi A., 2022, MNRAS, 512, 2508
Majumder P., Dutta B. G., Nandi A., 2024, MNRAS, 527, 4739
Majumder P., Dutta B. G., Nandi A., 2025, MNRAS, 540, 37
Merloni A., Vietri M., Stella L., Bini D., 1999, MNRAS, 304, 155
Migliari S., Belloni T., 2003, A&A, 404, 283
Morgan E. H., Remillard R. A., Greiner J., 1997, ApJ, 482, 993
Musoke G., Liska M., Porth O., van der Klis M., Ingram A., 2023, MNRAS, 518, 1656
Naik S., Rao A. R., Chakrabarti S. K., 2002, JA&A, 23, 213
Nandi A., Manickam S. G., Rao A. R., Chakrabarti S. K., 2001, MNRAS, 324, 267
Neilsen J., Remillard R. A., Lee J. C., 2011, ApJ, 737, 69
Niedźwiecki A., Zdziarski A. A., 2006, MNRAS, 365, 606
Nowak M. A., Wagoner R. V., Begelman M. C., Lehr D. E., 1997, ApJ, 477, L91
Reid M. J., McClintock J. E., Steiner J. F., Steeghs D., Remillard R. A., Dhawan V., Narayan R., 2014, ApJ, 796, 2
Remillard R. A., Morgan E. H., McClintock J. E., Bailyn C. D., Orosz J. A., 1999, ApJ, 522, 397
Ross R. R., Fabian A. C., Brandt W. N., 1996, MNRAS, 278, 1082
Singh K. P. et al., 2017, JA&A, 38, 29
Sreehari H., Ravishankar B. T., Iyer N., Agrawal V. K., Katoch T. B., Mandal S., Nand i A., 2019, MNRAS, 487, 928
Sreehari H., Nandi A., Das S., Agrawal V. K., Mandal S., Ramadevi M. C., Katoch T., 2020, MNRAS, 499, 5891
Strohmayer T. E., 2001, ApJ, 554, L169
Suková P., Janiuk A., 2015, MNRAS, 447, 1565
Taam R. E., Chen X., Swank J. H., 1997, ApJ, 485, L83
Titarchuk L., Seifina E., 2009, ApJ, 706, 1463
Vilhu O., Nevalainen J., 1998, ApJ, 508, L85
Vilhu O., Poutanen J., Nikula P., Nevalainen J., 2001, ApJ, 553, L51
Vincentelli F. M. et al., 2023, Nature, 615, 45
Zdziarski A. A., 2014, MNRAS, 444, 1113
Zdziarski A. A., Gierliński M., Rao A. R., Vadawale S. V., Mikołajewska J., 2005, MNRAS, 360, 825

This paper has been typeset from a TEX/LATEX file prepared by the author.